RSC Advances

PAPER

View Article Online
View Journal | View Issue

Cite this: *RSC Adv.*, 2026, **16**, 21346

On the thermal stability and surface and catalytic properties of Ag–Ni nanoparticles

Richard Fleischer, Pavel Brož, * Vít Vykoukal, Lucie Šimoníková, Petr Macháč, Markéta Holá and Jiří Sopoušek

Nanoparticles, due to their unique size-dependent properties, distinct from those of bulk materials, have become a rapidly developing and intensively studied area of chemistry. These properties include the ability to catalyse chemical reactions, reduced melting temperatures, and distinctive optical characteristics. In this paper, we investigate these features in bimetallic Ag@Ni core–shell nanoparticles of varying composition. The nanoparticles were synthesised *via* a solvothermal method using silver nitrate and nickel(II) acetylacetonate in a mixture of oleylamine and octadec-1-ene as solvents. Characterisation was carried out using a series of spectroscopic and microscopic methods. Catalytic activity and surface processes leading to the production and release of carbon dioxide were examined using Knudsen effusion mass spectrometry (KEMS). The highest catalytic activity was noted for Ag–Ni nanoparticles containing approximately 30–50 at% silver. The catalytic process is accompanied by the formation of organometallic compounds, which were detected by X-ray photoelectron spectroscopy (XPS) and laser ablation-inductively coupled plasma mass spectrometry (LA-ICP-MS). Thermal stability during heating was evaluated by differential scanning calorimetry (DSC), and a melting point depression of approximately 10 °C was observed for all studied samples. The paper is a part of a broader study of Ni-based bimetallic nanoparticles, their thermal stability and catalytic activity.

Received 25th February 2026
Accepted 7th April 2026

DOI: 10.1039/d6ra01654e

rsc.li/rsc-advances

Introduction

Nanoparticles, thanks to their size-dependent properties distinct from bulk materials, have become an intensively studied and rapidly developing field of chemistry. Among these properties, their ability to catalyse various chemical reactions is particularly noteworthy.

A reduction in particle size leads to an increased proportion of surface atoms with unsaturated bonds, which in turn results in higher surface energy of nanoparticles. Elevated surface energy leads to higher reactivity, as the atoms tend to lower their energy by forming new bonds.[1] The catalytic activity of Ag–Ni nanoparticles has been previously investigated on the following processes: methanol electrooxidation,[2] reduction of 4-nitrophenol and 4-nitroaniline,[3] nitroarene reduction,[4] synthesis of aromatic azo derivatives,[5] degradation of organic dyes,[3,6,7] glucose oxidation,[8] formate oxidation,[9] hydrogen generation,[10–12] sustainable nitrile hydration,[12] methane dry reforming with CO_2 participation[13] or oxygen evolution reaction.[14]

Another property that differs between nanoparticles and the bulk material of the same chemical composition is their lower temperature of phase transformation, also called melting point depression (MPD). This property is size-dependent, which means that the smaller the particle gets, the lower its temperature of phase transformation is.[15,16] MPD of Ag@Ni core–shell nanoparticles was studied for example by Vykoukal *et al.*[17]

In this study, the catalytic phenomena occurring on the surface of nanoparticles, as well as their thermal stability upon heating, were investigated. The entire composition range of the Ag–Ni system was examined. Catalytic activity of the prepared samples was evaluated using Knudsen effusion mass spectrometry (KEMS), focused on the evolution of CO_2 and other decomposition by-products from the organic layer on the surface of nanoparticles. Thermal stability of nanoparticles was assessed by differential scanning calorimetry (DSC), which was also employed to determine the MPD of selected samples.

This work builds upon and extends our previous research in the field of thermal stability and catalytic activity of Ni-based bimetallic nanoparticles[18] with the aim to complete the results for the Ag–Ni system.

Bimetallic Ag–Ni system

Silver and nickel form a binary system consisting of two solid solutions with a face-centred cubic (FCC) crystal structure. Despite the fact that both components of this system share the same crystal lattice, they exhibit only very limited mutual solubility. This restricted miscibility arises from the difference in atomic radius, different electronic structure of atoms, and

Masaryk University, Faculty of Science, Department of Chemistry, Brno, Czechia. E-mail: broz@chemi.muni.cz

positive enthalpy of mixing. According to the Ag–Ni phase diagram (Fig. S1), a monotectic reaction occurs at 1430 °C and a eutectic reaction at 961 °C, the latter temperature being close to the melting point of pure silver. The diagram also reveals the presence of a phase consisting of two conjugated liquid solutions, while no intermetallic phases are present in this system.[19,20]

Materials and methods

The nanoparticles were synthesized *via* the solvothermal hot-injection method, following the procedure described in ref. 21. Nickel(II) acetylacetonate and $AgNO_3$ in varying ratios were dissolved in the mixture of octadec-1-ene (ODE) and oleylamine (OAm) under a nitrogen atmosphere. OAm was used as the solvent due to its dual role as both a reducing agent and surfactant. In total, eight samples of bimetallic nanoparticles, ranging from 9 to 94 at% Ag, and two samples of pure metals were prepared for catalytic activity measurements using KEMS. For the thermal stability study by DSC, three nanoparticle samples were prepared.

Initial characterisation of synthetized nanoparticles was performed immediately after synthesis using ultraviolet-visible spectroscopy (UV-Vis) and dynamic light scattering (DLS) techniques.

UV-Vis spectroscopy was employed to investigate the presence of surface plasmon resonance (SPR). Absorption spectra were recorded using a Unican UV4 spectrophotometer (Chromspec). This double-beam scanning instrument employs a deuterium lamp for the UV range and a tungsten lamp for the visible range. A photomultiplier tube was used as the detector, with samples placed in quartz cuvettes. The nanoparticles were dispersed in cyclohexane, which also served as the blank. Absorbance measurements were carried out over the wavelength range of 220–800 nm. The absorbance values were normalized to the initial value at 220 nm, ensuring that all spectra started at the same point, and the relative absorbance was plotted in the final graph.

The hydrodynamic size of the prepared nanoparticles was determined using a Zetasizer Nano ZS instrument (Malvern Instruments), capable of measuring particles ranging from 0.3 nm to 10 μm. The nanoparticle dispersion in cyclohexane was filtered through a 450 nm pore-size PTFE filter and measured at room temperature in a square glass cuvette.

Particle size was analysed using a ThermoFisher Scientific F200C transmission electron microscope (TEM), operating at an accelerating voltage of 200 kV. A 4k × 4k CCD camera was used for image acquisition, and nanoparticle samples were deposited onto copper grids coated with a carbon film. For the determination of average particle size, approximately 700 particles were measured for each sample using Lince software.

Scanning electron microscopy (SEM) images were acquired using an Apreo 2S microscope (ThermoFisher Scientific), equipped with the Trinity Detection System comprising three detectors (T1, T2, T3), CBS (concentric backscattered), STEM (scanning transmission electron microscopy), and ETD (Everhart–Thornley) detectors. Imaging can be performed under either electrostatic or magnetic (immersion) field conditions. Elemental analysis was carried out using a TrueSight EDS detector in combination with ChemiSEM 2.0 software.

To determine the composition of the samples before and after KEMS/DSC analysis, elemental analysis was performed using an iCAP PRO inductively coupled plasma optical emission spectrometer (ICP-OES, ThermoFisher Scientific). The samples were dissolved in 65% HNO_3 and subsequently diluted with deionised water.

To investigate coating after KEMS measurements formed by condensation of vapours in colder parts of the Knudsen cell and ceramic radiation shields of the carrier, X-ray photoelectron spectroscopy (XPS) and laser ablation – inductively coupled plasma mass spectrometry (LA-ICP-MS) were used. The XPS measurements were performed on a Kratos Axis Supra device equipped with a monochromatic X-ray source with Al Kα (E = 1486.6 eV) excitation. A binding energy of 284.8 eV for C 1s was used for calibration. Ag, Ni and C in a form of various functional groups was monitored. The LA-ICP-MS measurements were performed to monitor Ag and Ni. To assess the elemental background associated with deposits formed during the heating experiments, additional elements including Mg, Al, Ti, V, Cr, Mn, Fe, Cu, Zn, Nb, Ta and Pb were monitored. The system consisted of an LSX-213 G2+ (Teledyne CETAC) laser ablation device coupled to an ICP-MS Agilent 7900 (Agilent Technologies) equipped with a quadrupole analyser and an octopole reaction cell. The laser operated at a wavelength of 213 nm with a pulse duration of ≤4 ns, using a two-volume HelEx II ablation cell. Line scans were performed with a spot size of 100 μm in diameter, a repetition rate of 10 Hz, a fluence of 2 J cm^{-2} and a scan speed of 10 μm s^{-1}.

The catalytic properties of the nanoparticles were investigated by KEMS using a Netzsch STA 409 CD/3/403/5/G instrument in a Knudsen cell from alumina. Temperature calibration was performed using the melting points of a series of pure metals, as described in ref. 18. The mass spectrometer was calibrated using 5,7-dibromo-8-hydroxyquinoline (broxyquinoline) as the standard. To evaluate the catalytic decomposition of oleylamine (OAm) in the presence of nanoparticles, the mass spectrum of pure OAm was also recorded as a reference control experiment. Prior to measuring each nanoparticle sample, a baseline mass spectrum was acquired with an empty Knudsen cell as a blank control experiment. During measurements, the apparatus was maintained under vacuum at approximately 1 × 10^{-3} Pa. The temperature program applied involved heating the sample at a rate of 5 K min^{-1} up to 1000 °C, followed by cooling at 10 K min^{-1} down to 600 °C, and further cooling at 20 K min^{-1} to 30 °C. Sample masses of 2 mg and 3 mg were used for broxyquinoline and OAm, respectively, whereas 5 mg of sample was used for nanoparticle measurements. The key peaks monitored in the nanoparticle spectra were selected based on the characteristic and significant peaks observed in the spectra of oleylamine (OAm), octadec-1-ene (ODE), and their oxidative decomposition products, octadec-14-en-1-al and oleylnitrile. The following mass spectral regions were selected for detailed analysis: 38–170, 175–185, 188–198, 203–225, 230–246, 260–274. Despite rigorous vacuum conditions, residual oxygen molecules

remained present, allowing oxidative processes to occur on the nanoparticle surfaces during heating.

Thermal stability of both the organic shell and the nanoparticles was assessed using a Netzsch STA 409 CD/3/403/5/G instrument. The analysed sample was placed in a DSC crucible from alumina, while an empty crucible from the same material served as the reference. Both crucibles were positioned on a shared platinum platform, each directly above an individual thermocouple. Measurements were performed under a high-purity argon atmosphere (6N). Prior to entering the furnace, the argon flow was purified of residual oxygen in an external furnace (Supelco Analytical 29546-U by Thermocraft, Inc.) by passing through a heated zirconia tube, and further purified inside the furnace by a zirconia getter located directly beneath the DSC crucibles. The temperature program consisted of three heating–cooling cycles. In each cycle, the sample was heated to 1100 °C. Cooling was carried out to 50 °C in the first and second cycles, and to 30 °C in the final cycle. Both heating and cooling rates were set to 10 K min^{-1}. To obtain a sufficient amount of nanoparticles for DSC analysis, the synthesis was conducted using double amount of precursors.

Results and discussion

Ag–Ni sample characterisation

The synthesised Ag–Ni, Ag, and Ni nanoparticles (NPs) were characterised using the methods summarised in Table 1. In the following chapter, the term "sample name", defined according to the atomic percentage of metals, will be used when discussing the results. Selected samples were also examined by SEM–EDS following their analysis by KEMS and DSC.

The composition of the synthesised samples was determined by elemental analysis of nanoparticle solutions using inductively coupled plasma optical emission spectroscopy (ICP-OES). The actual composition of the nanoparticles showed slight deviations from the intended values. These discrepancies may have arisen from incomplete dissolution of the precursors or from precipitation and deposition of material on the walls of the reaction vessel, as well as inside the needle and syringe used to inject the precursor solution into the reaction vessel during synthesis.

From the data presented in Table 1, the average size of the bimetallic nanoparticles ranged from 9.9 nm to 17.6 nm, with standard deviations between 2.2 nm and 5.8 nm, indicating a relatively narrow size distribution for each sample. In contrast, the nickel nanoparticles exhibited a substantially larger mean size of nearly 30 nm, accompanied by a higher standard deviation, suggesting the presence of a broader range of particle sizes, including larger particles.

A similarly increased size was observed for the neat silver sample. Although its mean size is reported as 56.2 nm with a standard deviation of 23 nm, this value does not fully reflect the actual morphology, as it was determined solely from clearly distinguishable individual nanoparticles, which were limited in number, as seen in the STEM image of this sample (Fig. S2). The image and subsequent size analysis revealed the coexistence of isolated nanoparticles and agglomerates reaching several hundred nanometres in size. Notably, comparison with the size obtained by dynamic light scattering (DLS) immediately after synthesis shows that the Z-average for this sample (Ag) was 21 nm. This suggests that aggregation may have occurred gradually between the synthesis and the STEM analysis. In the Fig. 1, example of $Ag_{29}Ni_{71}$ nanoparticles sample is shown.

Dynamic light scattering (DLS) measurements provided the hydrodynamic size of the nanoparticles, *i.e.*, the size of the metallic cores together with their organic shells. The *Z*-average values and polydispersity index's (PdI) are summarised in Table 1 along with the identification of the analytical method used for each sample. As seen in the table, the hydrodynamic size can vary substantially depending on the amount of organic material present on the nanoparticle surface. This variation is influenced by both the synthesis conditions and the post-synthesis washing process. The Z-average values obtained by DLS ranged from 17 nm to 65 nm.

Table 1 clearly shows that the size of the bimetallic nanoparticles does not depend on their composition and that these

Table 1 Results of Ag–Ni, Ag and Ni NPs characterisation

		Size of metallic core (TEM, STEM)		Hydrodynamic diameter (DLS)		
Sample name	Composition ICP-OES Ag : Ni [at%]	Diameter [nm]	$\pm\delta$ [nm]	*Z*-Diameter [nm]	Polydispersity index (PDI)	Method of investigation
Ni	Ni	29.7	7.2	68.8	0.523	KEMS
Ag_9Ni_{91}	8.7 : 91.3	14.9	3.0	28.0	0.236	
$Ag_{29}Ni_{71}$	28.5 : 71.5	12.6	2.8	22.0	0.293	
$Ag_{35}Ni_{65}$	34.5 : 65.5	10.2	2.8	10.8	0.228	
$Ag_{45}Ni_{55}$	44.8 : 55.2	9.9	3.1	16.8	0.108	
$Ag_{62}Ni_{38}$	62.2 : 37.8	11.8	2.4	22.4	0.206	
$Ag_{73}Ni_{27}$	72.7 : 27.3	10.2	2.5	59.4	0.403	
$Ag_{94}Ni_6$	94.4 : 5.6	17.6	5.8	46.0	0.268	
Ag	Ag	56.2	23.0	21.3	0.116	
Ag_9Ni_{91}	9.3 : 90.7	10.9	2.2	26.5	0.270	DSC
$Ag_{51}Ni_{49}$	50.9 : 49.1	13.9	4.3	65.1	0.136	
$Ag_{86}Ni_{14}$	85.6 : 14.4	13.9	3.0	26.8	0.294	

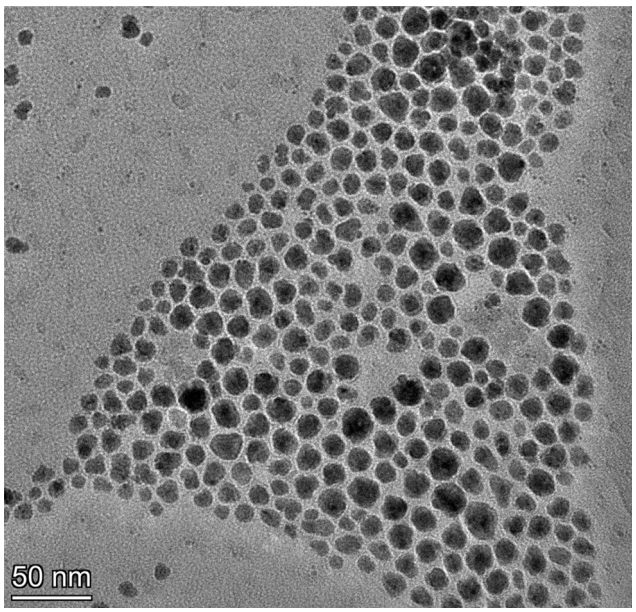

Fig. 1 TEM image of $Ag_{29}Ni_{71}$ sample.

nanoparticles exhibited a smaller average size compared to those composed of the pure elemental metals.

The presence of surface plasmon resonance (SPR) was investigated using UV-Vis spectroscopy, and the spectra showing the dependence of relative absorption on wavelength for each sample are presented in Fig. 2. Absorption spectra were recorded over the wavelength range of 220–800 nm. Silver nanoparticles exhibited a distinct localised absorption maximum at approximately 400 nm. Absorption in the 220–280 nm range corresponds to oleylamine (OAm), with its intensity depending on the concentration of OAm on the nanoparticle surface. As can be seen, almost all samples displayed an absorption maximum within the range of 400–420 nm. The position of the SPR peak can be influenced by the nanoparticle size, composition and shape.[22–27] The sample containing 9 at% Ag (grey curve) showed no detectable SPR, most likely due to the low silver content.

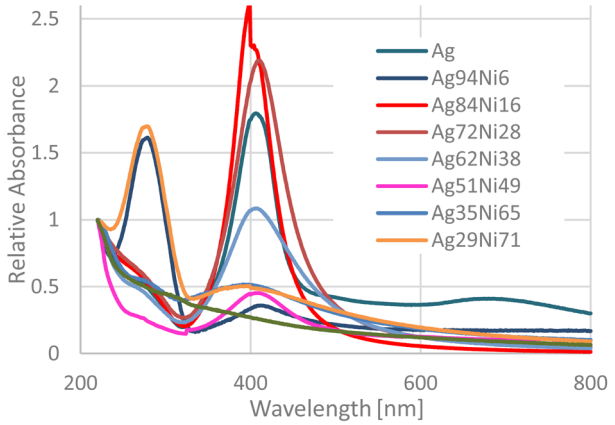

Fig. 2 Relative UV-Vis absorption spectra of selected AgNi NPs.

Surface properties and catalytic activity

To evaluate the dependence of catalytic activity on the nanoparticle composition, a series of samples covering the whole concentration region was investigated by the KEMS method. The activity was evaluated against the measurement of background with an empty Knudsen cell. The pure oleylamine was measured as well. Every sample was weighed before and after KEMS analysis, and the results are shown in Table S1. Before analysis, the sample had the look of black powder, and after analysis, the colour was changed to greyish. The observed mass loss likely corresponds to the products of catalytic decomposition of the organic shell on the nanoparticle surface, which subsequently evaporated into the mass spectrometer. As shown in the Table S1, the smallest mass loss was recorded for the samples composed of the elemental metals.

In the first selected mass spectrum range, two dominant peaks were observed in the KEMS spectra of all samples. The first peak, at 40 amu, corresponds to argon, which was present both during apparatus cleaning and when the chamber was opened for sample insertion. Despite intensive evacuation of the system, residual argon was consistently detected during analysis. The second dominant and, for the purposes of this study, more relevant peak appears at 44 amu. This peak corresponds to CO_2, formed *via* oxidation of organic species on the nanoparticle surface. Carbon dioxide production was evident in the spectra of all nanoparticle samples except for the Ag sample, which was partially aggregated. In the spectrum of the $Ag_{29}Ni_{71}$

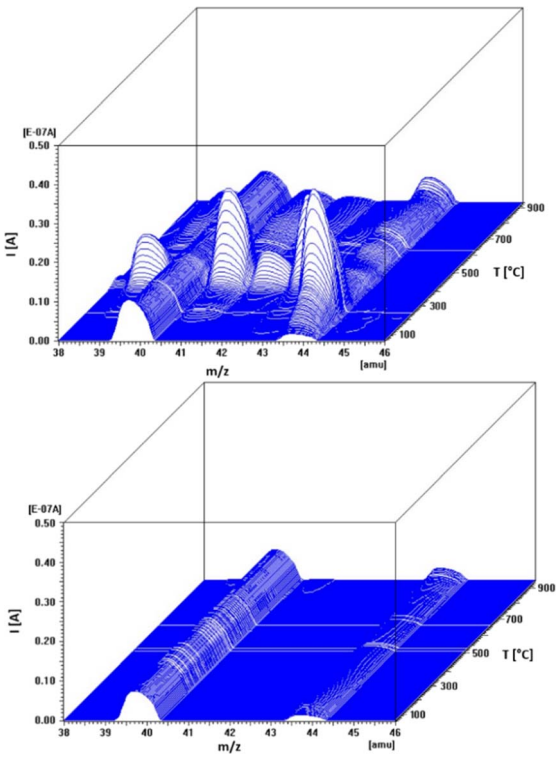

Fig. 3 Mass spectrum of $Ag_{29}Ni_{71}$ nanoparticles in the m/z range 38–46 (top: sample spectrum; bottom: background). The peak at m/z = 40 corresponds to residual argon, while the peak at $m/z = 44$ indicates CO_2 evolution.

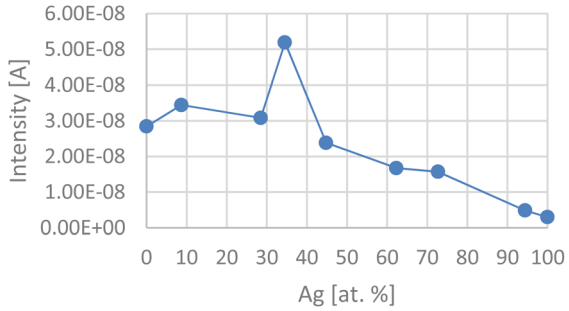

Fig. 4 Dependence of the CO_2 (m/z 44) signal intensity on the silver content in the sample.

sample (Fig. 3), low-mass organic fragments are clearly visible. Weak signals of such fragments were also observed for the $Ag_{45}Ni_{55}$, $Ag_{73}Ni_{27}$, and, to a lesser extent, $Ag_{62}Ni_{38}$ samples.

The blank control experiment with an empty Knudsen cell and the reference control experiment with pure oleyamine did not show any such signals. The results of the measurement of pure oleylamine are reported in ref. 18.

The CO_2 formation occurs for all samples within a similar temperature range of approximately 100–250 °C, with the peak maximum located between ~180 °C and 220 °C. Fig. 4 compares the background-corrected CO_2 signal intensities as a function of sample composition.

The trendline in Fig. 4 shows that the signal intensity increases toward the sample containing 34.5 at% Ag, which exhibits a significantly higher intensity than the other samples (*i.e.*, a local maximum, see Fig. S3).

Overall, an inverse relationship is observed between silver content and CO_2 signal intensity, with the latter decreasing as the Ag fraction increases.

In the second selected mass spectrum range (m/z 46–110), signals corresponding to the decomposition products of the organic nanoparticle shell were monitored. All samples exhibited signals around 400 °C. Peaks in this temperature range displayed a relatively similar pattern across the samples, differing primarily in intensity. Significantly higher signals, up to an order of magnitude greater than those of the other samples, were observed for the $Ag_{29}Ni_{71}$ sample (Fig. 5). As described in the subsequent part, this sample also produced high-intensity fragment signals in other mass ranges. In contrast, significantly lower signals were detected for the elemental nickel sample as well as for $Ag_{67}Ni_{33}$ and $Ag_{94}Ni_6$.

The m/z range of 110–170 was monitored in the third section of the mass spectra. Similar to the previous range, fragment signals from the organic shell are predominantly observed around 400 °C. However, some samples also show signals at lower temperatures, near 200 °C. The elemental Ni sample, as well as $Ag_{67}Ni_{33}$ and $Ag_{94}Ni_6$, exhibit the lowest signal intensities. In contrast, the $Ag_{29}Ni_{71}$ sample again shows signals up to one order of magnitude higher than the other samples in this range.

The m/z range of 175–185 was the next region of interest. The spectral profiles of all samples were generally similar, with maximum signal intensities again observed around 400 °C. In

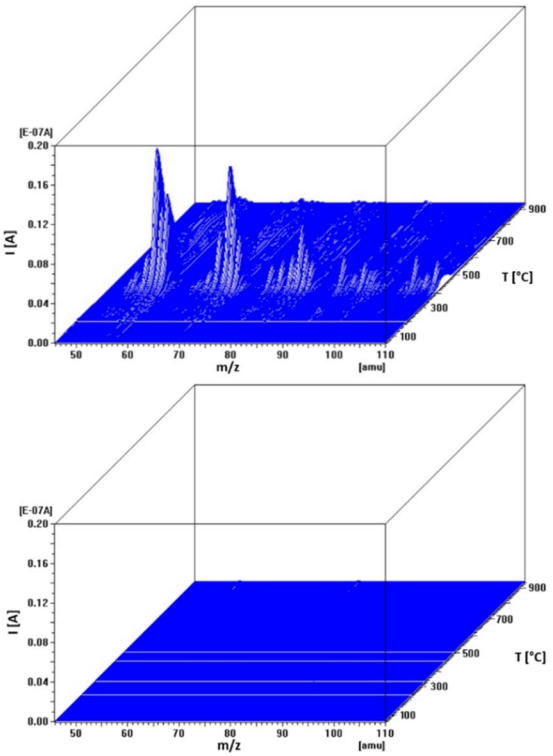

Fig. 5 Mass spectrum of $Ag_{29}Ni_{71}$ nanoparticles in the m/z range 46–110 (top: sample spectrum; bottom: background), illustrating the evolution of decomposition products from the organic nanoparticle shell.

some cases, the onset of the peaks could be traced at lower temperatures, around 150–200 °C. The elemental Ni sample exhibited the lowest signal intensities within this range. The $Ag_{29}Ni_{71}$ sample again showed signals approximately one order of magnitude higher than those of the other samples. Relatively high signal intensities were also observed for the $Ag_{73}Ni_{27}$ sample.

In the m/z range of 188–198, the spectra of all samples were relatively similar, showing no discernible trends. Consequently, these spectra are not included in this study. Within this range, the elemental Ni sample exhibited the lowest signal intensities, whereas the $Ag_{29}Ni_{71}$ sample showed the highest intensities.

In the sixth m/z range (203–225), the primary peak of interest was observed at m/z 207, corresponding to octadec-14-en-1-al, an oxidation product of ODE. The formation of this product has been reported in previous work.[18] This peak is clearly visible in the spectra of all samples except for the elemental Ni nanoparticles, where it merges with the background. Oxidation of ODE to octadec-14-en-1-al generally occurs around 150–200 °C, although in some cases the maximum signal intensity is again observed near 400 °C. Samples $Ag_{29}Ni_{71}$ and $Ag_{73}Ni_{27}$ (Fig. 6) exhibit more pronounced fragmentation of organic compounds, with signals appearing at m/z values where other samples show little or no response.

A comparison of the m/z 207 peak intensity, corresponding to octadec-14-en-1-al, as a function of sample composition is shown in Fig. 7. Signal intensities were again corrected for background.

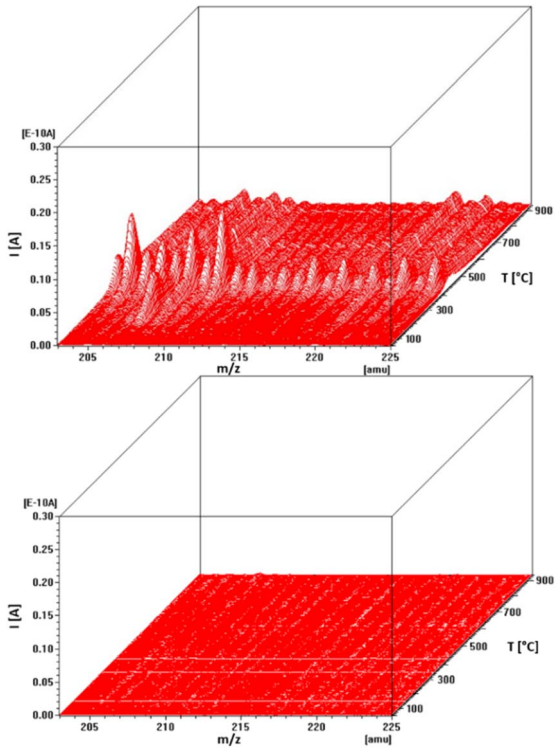

Fig. 6 Mass spectrum of $Ag_{73}Ni_{27}$ nanoparticles in the *m*/*z* range 203–225 (top: sample spectrum; bottom: background).

From the dependence shown in Fig. 7, it can be seen that the sample containing 35 at% Ag exhibited the lowest octadec-14-en-1-al (*m*/*z* 207) signal. This is the same sample that displayed the highest CO_2 signal (Fig. 4). Fig. 7 also shows that while the elemental Ni nanoparticles produced the lowest octadec-14-en-1-al signal, the partially aggregated elemental Ag sample provided the second-highest octadec-14-en-1-al signal.

In the *m*/*z* range of 230–246, the elemental Ni nanoparticles exhibited no detectable signals. Minimal signals were also observed for the $Ag_{94}Ni_6$ sample and the elemental Ag sample. The most prominent signals were recorded for the $Ag_{29}Ni_{71}$ sample, followed by the $Ag_{73}Ni_{27}$ sample. No clear trend was observed within this *m*/*z* range, and therefore the corresponding spectra are not shown.

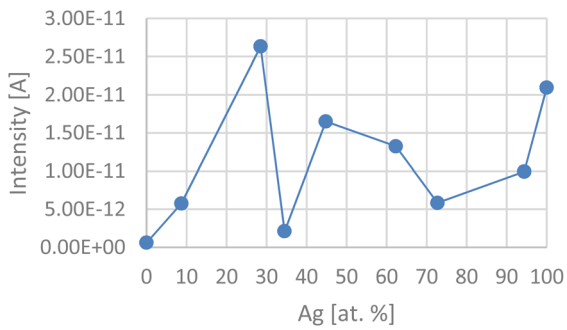

Fig. 7 Dependence of the octadec-14-en-1-al (*m*/*z* 207) signal intensity on the silver content in the sample.

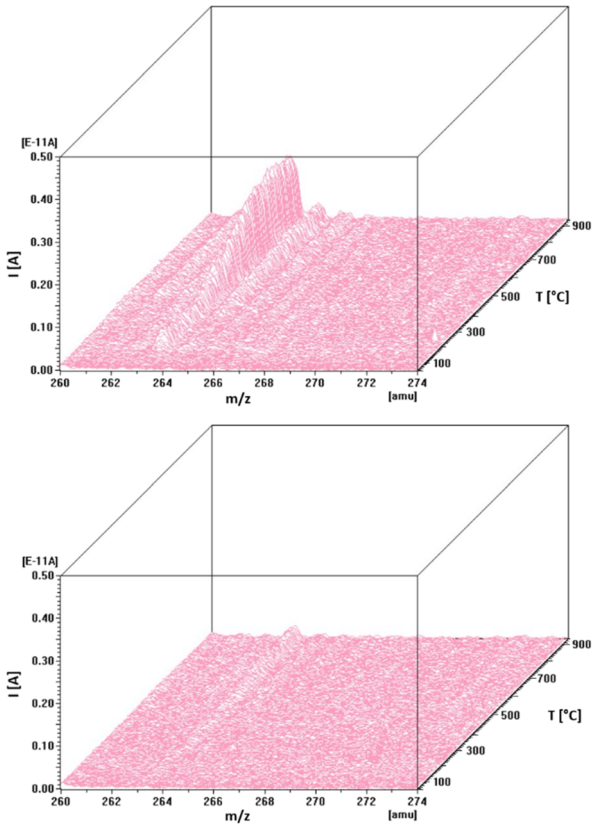

Fig. 8 Mass spectrum of $Ag_{35}Ni_{65}$ nanoparticles in the *m*/*z* range 260–274 (top: sample spectrum; bottom: background).

The final investigated *m*/*z* range was 260–274. Within this range, the peaks at *m*/*z* 263 and 267 were of primary interest. The peak at *m*/*z* 263 corresponds to oleylnitrile, an oxidation product of OAm. No discernible peak was observed in the spectrum of elemental Ni nanoparticles, and only very small signals were detected for the elemental Ag sample. The highest oleylnitrile signal was recorded for the $Ag_{35}Ni_{65}$ sample (Fig. 8), followed by $Ag_{29}Ni_{71}$. The peak at *m*/*z* 267 corresponds to the molecular ion of OAm, which was clearly observed for the Ag and $Ag_{29}Ni_{71}$ samples. In the spectra of the remaining bimetallic samples, the molecular OAm peak exhibited either very low intensity or was absent. The dependence of the *m*/*z* 263 peak intensity on sample composition is shown in Fig. 9, with signals again corrected for background.

As also found, the mass spectra of the sample $Ag_{62.2}Ni_{37.8}$ in the investigated *m*/*z* ranges showed similar features to those published in our previous study.[18]

From the trend shown in Fig. 9, it is evident that the signal intensity of oleylnitrile increases from the elemental metals Ni and Ag toward the sample containing 35 at% Ag. This is the same sample that exhibited the highest CO_2 signal and the lowest octadec-14-en-1-al signal.

Fig. 10 summarizes the compositional trends observed in Fig. 4, 7 and 9, with dimensionless values plotted for clarity. Elemental Ni nanoparticles exhibited a relatively high CO_2 signal (fourth highest among nine samples), while the partially

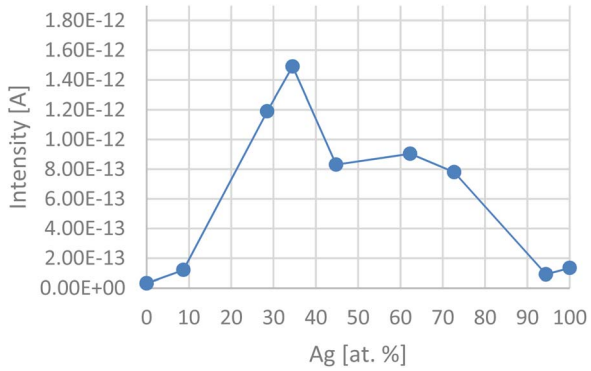

Fig. 9 Dependence of the oleylnitrile (*m*/*z* 263) signal intensity on the silver content in the sample.

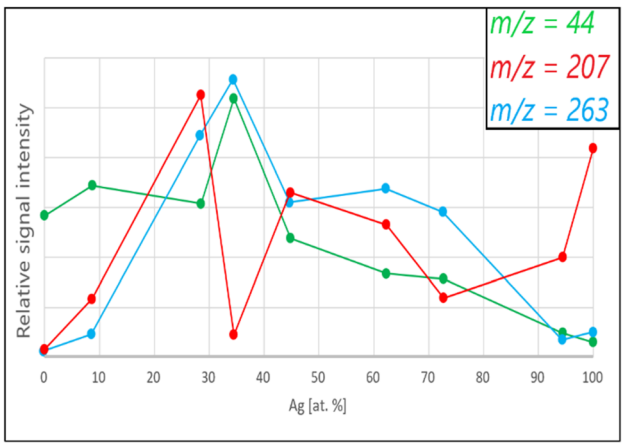

Fig. 10 Summary of the dependencies of selected *m*/*z* signals on the composition of the nanoparticle samples.

aggregated elemental Ag sample showed the second highest signal for octadec-14-en-1-al (*m*/*z* 207), the oxidation product of ODE. Both elemental metals produced only very low signals for oleylnitrile (*m*/*z* 263), the OAm oxidation product.

Mass spectra of elemental metals indicate generally higher signal intensities for Ag compared to Ni, which decreases with increasing *m*/*z*. For bimetallic samples, lower mass ranges ($m/z \leq 200$) show effective organic fragmentation, with differences primarily in intensity. The $Ag_{94}Ni_6$ sample exhibited the lowest signals, often below those of elemental Ag. At higher masses ($m/z \geq 200$), some samples displayed extensive fragmentation with several peaks of comparable intensity, while others showed limited fragmentation with only a few high-intensity peaks. Notably, $Ag_{29}Ni_{71}$ consistently produced the highest signals across most mass ranges, in some cases up to one order of magnitude higher than the other samples.

The catalytic activity of the nanoparticle samples was evaluated based on CO_2 evolution upon heating. The dependence of catalytic activity on sample composition is shown in Fig. 4. CO_2 is generated through the catalytic oxidation and decomposition of OAm and ODE on the nanoparticle surfaces, with other organic fragments detected at higher *m*/*z* values. The highest CO_2 production was observed for $Ag_{35}Ni_{65}$ nanoparticles, which exhibited a significantly stronger signal than the other samples, whereas $Ag_{29}Ni_{71}$ displayed the most intense organic fragment signals. Overall, nanoparticles containing 30–50 at% Ag demonstrated the highest catalytic activity, emphasizing a clear correlation between catalytic performance and sample composition, as summarized in Fig. 10.

The catalytic activity of AgNi nanoparticles depends strongly on their composition.[3,5] In ref. 3 and 5, activity was examined for the reduction of 4-nitrophenol to 4-aminophenol and the synthesis of azobenzene from aniline, respectively. In both cases, nanoparticles with 60 at% Ag and 40 at% Ni exhibited the highest activity, while compositions approaching the pure metals were less active.

In the present study, the highest catalytic activity was observed for nanoparticles containing 30–50 at% Ag. Although all studies indicate that bimetallic nanoparticles of specific compositions outperform other compositions, the optimal composition varies. The authors of ref. 2 and 3 reported that their nanoparticles exhibited a fivefold twinned morphology consisting of a solid solution in which Ni atoms are embedded in an Ag matrix. In contrast, nanoparticles prepared in this work using the employed synthesis method exhibit a core–shell Ag@Ni structure.[21] Differences in structure, and the resulting electronic interactions between elements, likely influence composition-dependent activity. Surface functionalization with organic stabilizers may also contribute, as it is known to play a critical role in catalytic performance.[28,29]

In addition to these findings, a formation of pinkish-brown coating was visually apparent on colder parts of the Knudsen cell and ceramic radiation shields of the carrier from condensation of vapours during the heating. Unlike our previous study of this system,[18] this coating has been studied in detail by means of XPS and LA-ICP-MS. The XPS measurements showed presence of Ag and C including bonds and functional groups such as C–C, C–O and C=O compared with clean ceramic parts before the KEMS measurement (see Table S2 as an example for alloy $Ag_{94}Ni_6$). The LA-ICP-MS revealed presence of Ag and only traces of other elements as the background. A notable presence of Al was observed, which is consistent with the Al_2O_3 composition of the ceramic radiation shields on which the condensates were deposited. In accordance with our earlier observation from the study of the Ag–Ni[18] and Ag–Cu[30] systems, creation of organometallic compounds and their consequent deposition take place during the heating process. It should be noted that no formation of such coating was observed in our recent studies focused on the Cu–Ni system.[18,31] As mentioned in ref. 18, the use of quadrupole mass analyser (QMS) which is known to discriminate intensities at especially high masses is difficult due to complexity of the catalytic process and hence the complexity of the organometallic compounds for the mass spectrometric monitoring. The state of the nanoparticles after KEMS analysis was characterized using SEM and SEM-EDS. Fig. 11 presents example for the $Ag_{35}Ni_{65}$ sample. The images reveal small, spherical particles embedded within a carbonaceous matrix, formed as a result of the pyrolysis of the organic shell. This matrix limited extensive coagulation and growth of the nanoparticles into larger agglomerates. The images further

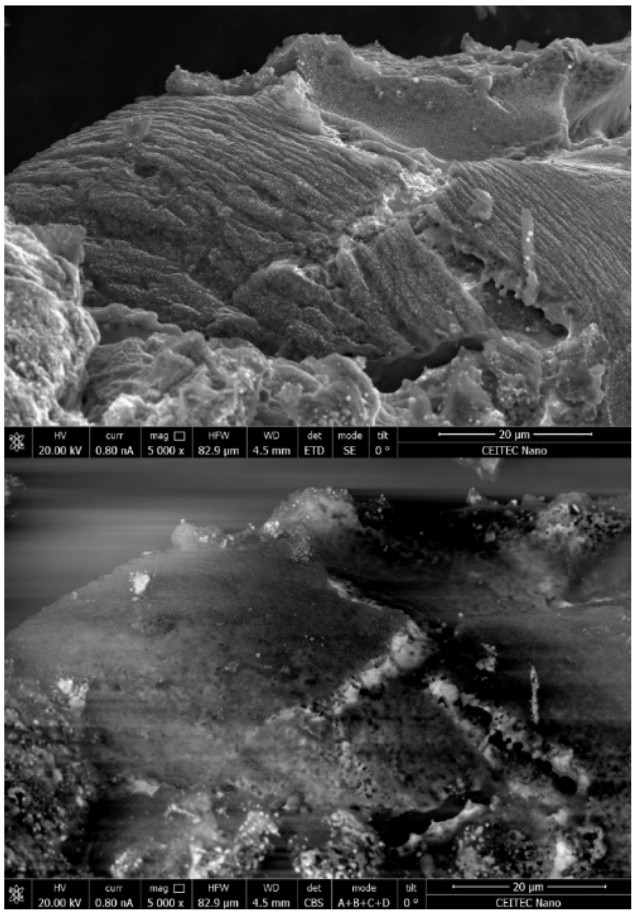

Fig. 11 SEM image of sample $Ag_{35}Ni_{65}$ after the KEMS analysis (top – ETD detector, bottom – CBS detector).

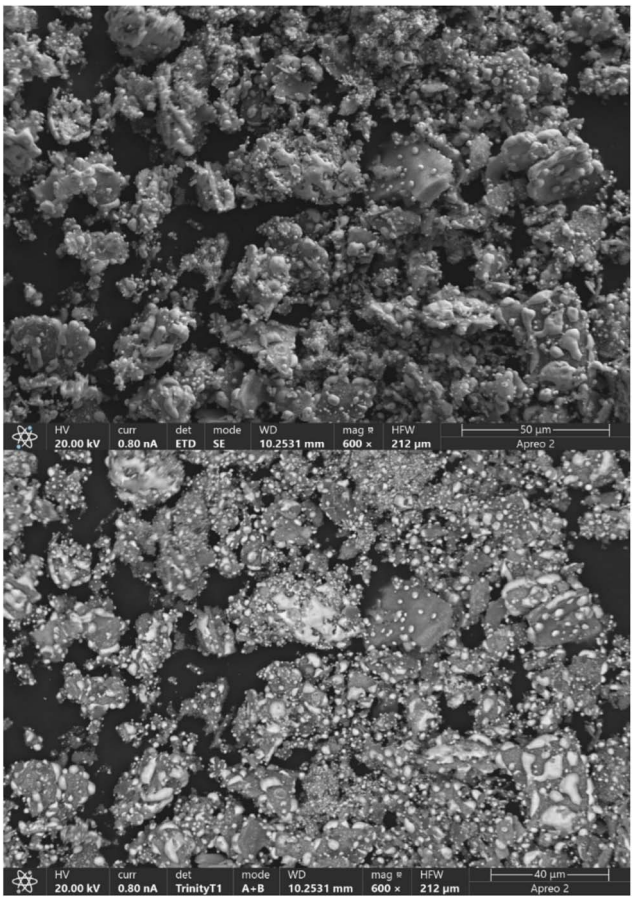

Fig. 12 SEM image of sample $Ag_{62}Ni_{38}$ after the KEMS analysis (top – ETD detector, bottom – CBS detector).

indicate that the nanoparticles largely retained their structural integrity. Considering the sample composition determined by ICP-OES ($Ag_{35}Ni_{65}$), it can be inferred that the nickel shell effectively encapsulated the silver core.

An opposite situation was observed for the $Ag_{62}Ni_{38}$ sample (Fig. 12), which represented the composition with the highest silver content among the analysed materials. The images show that particles are located both within and on the surface of the pyrolysis products. In addition to the presence of particles of different sizes, continuous regions enriched in silver are also visible. Given the relatively low nickel content, it can be assumed that nickel does not form a complete shell around the nanoparticles but rather small nickel-rich islands distributed on the surface of the silver particles. As a result, the silver cores are not fully encapsulated, and during heating they undergo coagulation, leading to the formation of silver-rich domains. Elemental analysis was carried out on selected areas and points of the sample. The results were visualized using the ChemiSEM™ technology, which provides information on both the composition and spatial distribution of elements within the sample. In this representation, individual elements are represented by a specific colour, with the colour intensity corresponding to their relative concentration. Example of EDS analysis for the $Ag_{62}Ni_{38}$ sample is shown in Fig. S4–S6.

Thermal stability

Differential scanning calorimetry (DSC) was used to investigate the thermal stability of samples containing 9.3, 50.9, and 85.6 at% silver. The aim was to determine the decrease in the phase transformation temperature, which for bulk material occurs at 961.1 °C.[32] The mass of the nanoparticles before and after thermal analysis is summarized in Table S3.

Endothermic effects were observed in the DSC traces of all three samples already at lower temperatures. These effects can be attributed to the decomposition and evaporation of the organic shell surrounding the nanoparticles, consistent with the recorded mass loss during analysis. An endothermic peak in the range of 200–240 °C was assigned to CO_2 formation. In comparison, KEMS analysis revealed the onset of CO_2 release at lower temperatures (approximately 100–150 °C). This discrepancy is likely due to methodological differences: KEMS is performed under vacuum at low pressure, whereas DSC is conducted under atmospheric pressure in an inert atmosphere.

The DSC curve for the Ag_9Ni_{91} sample is shown in Fig. 13. At lower temperatures, a double endothermic peak was observed at 209.4 °C and 240.3 °C, which can be attributed to CO_2 evolution. The broad, split character of the peak likely reflects CO_2 release from different regions of the sample. A depression of the melting temperature was consistently observed in all

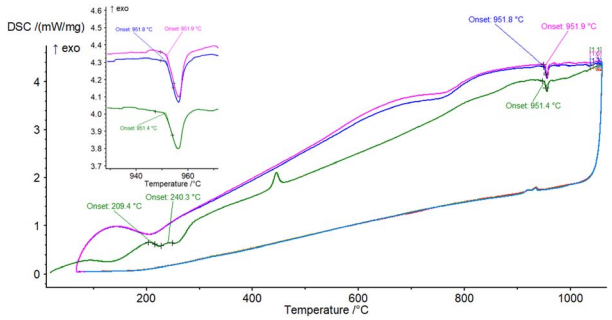

Fig. 13 DSC curve of the Ag_9Ni_{91} sample. The inset highlights the region around the melting temperature. The first heating cycle is shown in green, the second in blue, and the third in violet.

three heating cycles, with the nanoparticle melting point measured to be approximately 10 °C lower than that of the bulk alloy. The melting temperatures between successive cycles showed only minor variations, indicating the persistence of a nanoparticle fraction even after three heating and cooling cycles. This stability is likely maintained by the Ag@Ni core–shell structure and the protective carbon matrix formed through pyrolysis of the organic shell, as further discussed for the second sample.

An additional exothermic peak was detected at ~430 °C. The origin of this feature remains unclear and may involve processes specific to the nanoparticle system, warranting further investigation. On the cooling curves, small exothermic peaks associated with the solidification of the molten phase were visible. Their shapes were consistent across all three cycles and appeared as doublets, each component corresponding to the solidification of a distinct nanoparticle size fraction.

The second DSC curve, corresponding to the $Ag_{51}Ni_{49}$ sample, is presented in Fig. 14. The record shows only a minor endothermic peak at 236.0 °C, attributed to CO_2 evolution. In the melting region, broad double peaks were observed in each heating cycle. The presence of such wide double peaks can be explained by the existence of distinct particle size fractions that undergo melting successively. SEM images of the sample are shown in Fig. S7. The micrograph reveals small nanoparticles embedded within the carbon matrix, as well as a single large particle exceeding 300 μm in size. EDS analysis confirmed that the surface of this large particle is predominantly composed of silver. The melting temperatures of the two components of the split peak varied only slightly between individual cycles, indicating the persistence of a nanoparticle fraction even after repeated heating and cooling.

This behaviour can be rationalized by two contributing factors. First, the core–shell architecture of the nanoparticles, in which silver forms the core encapsulated by a nickel shell, provides partial protection of silver against coalescence. However, the nickel shell is not always structurally perfect, and unprotected silver domains may still undergo aggregation. Second, the presence of pyrolysis products from the organic capping agents likely contributes to the stabilization of the particles. These species form a carbonaceous matrix around the nanoparticles, which effectively hinders their coalescence into larger entities. Consequently, similar melting temperatures were recorded across all three cycles. The carbonaceous matrix also ensures the preservation of a sufficient fraction of the original nanoparticles, reflected in the consistently reduced melting point relative to the bulk alloy.

The first set of melting temperatures (948.5–951.2 °C) correlates well with the records of the other two samples and can be attributed to the melting of nanoparticles, accompanied by a melting point depression of approximately 10–12 °C relative to the bulk alloy. The second observed melting event occurs closer to the bulk melting temperature and is associated with a fraction of aggregated nanoparticles or larger particles. On the cooling curves, pronounced and sharp exothermic peaks corresponding to the solidification of the molten phase were detected. The most intense peak was observed during the final cooling cycle, consistent with progressive homogenization of the sample upon repeated heating and cooling.

The DSC trace of the $Ag_{86}Ni_{14}$ sample is shown in Fig. 15. An endothermic peak observed at 240.2 °C is associated with the catalytic formation of CO_2. A second endothermic feature at 436.2 °C, absent in the previous two samples, is likely related to the formation of products arising from the catalytic decomposition of surface-bound organic species.

In the first heating cycle, two distinct endothermic peaks were detected in the melting region, at 946.3 °C and 952.7 °C. In contrast, the second and third cycles exhibited single melting peaks with intermediate positions between the two values

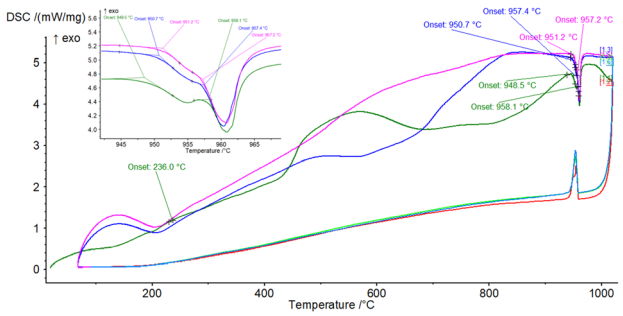

Fig. 14 DSC curve of the $Ag_{51}Ni_{49}$ sample. The inset highlights the region around the melting temperature. The first heating cycle is shown in green, the second in blue, and the third in violet.

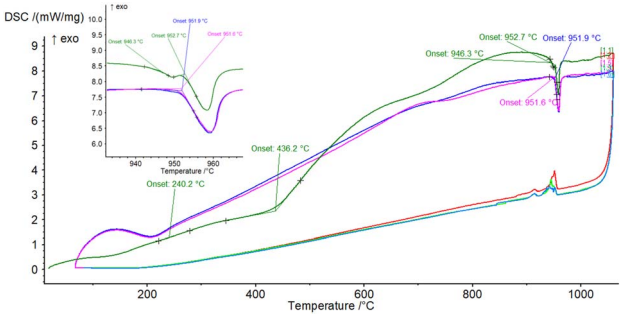

Fig. 15 DSC curve of the $Ag_{86}Ni_{14}$ sample. The inset highlights the region around the melting temperature. The first heating cycle is shown in green, the second in blue, and the third in violet.

recorded in the first cycle. The melting peaks in the second and third cycles were nearly identical, differing by only 0.3 °C. This behaviour suggests that during the first heating cycle, the sample underwent partial remelting and homogenization, leading to the disappearance of the smallest nanoparticle fraction and the formation of broader size distributions. This process likely caused both the peak broadening and the slight shift toward higher temperatures.

The maximum melting point depression, nearly 15 °C relative to the bulk alloy, was observed during the first cycle. In the second and third cycles, the melting point depression stabilized at approximately 10 °C, consistent with the observations for the other samples.

Table 2 summarizes the measured temperatures of the endothermic effects for the individual samples and compares them with the melting temperature of the bulk alloy.

Based on the data summarized in Table 2, all analysed samples exhibited a reduced melting temperature across all three heating cycles, with a decrease of more than 10 °C compared to the bulk material. As discussed above, this reduction is likely attributable to the Ag@Ni core–shell structure of the nanoparticles and the presence of a carbon matrix. During the first heating cycle, pyrolysis of the organic ligands on the nanoparticle surfaces leads to the formation of a carbon matrix, in which nanoparticles are embedded both on the surface and within the matrix. While nanoparticles with incomplete nickel shells on the matrix surface may aggregate into larger particles or compact structures upon heating, those embedded within the matrix remain fully or partially protected against aggregation. This mechanism explains why a decreased melting temperature, associated with a broad endothermic peak, was observed even after three heating cycles.

In some cases, the endothermic peaks were split, yielding two distinct melting temperatures. The splitting and the overall width of the endothermic peaks reflect the presence of nanoparticle fractions of different sizes, as nanoparticles of varying dimensions melt at different temperatures.

The measured melting point depression of Ag@Ni nanoparticles in this work is in good agreement with data reported in ref. 17. The cited study investigated Ag@Ni nanoparticles of varying compositions with average sizes ranging from 10.9 to 15.5 nm. The melting temperatures recorded in the first heating cycle ranged from 944.3 °C to 948.9 °C. A reduction in melting temperature was observed across all three cycles, with only minimal variation between cycles, consistent with the findings of the present study. Considering the differences in composition and particle size between the samples analysed here and those reported in the literature, the results are in good overall agreement.

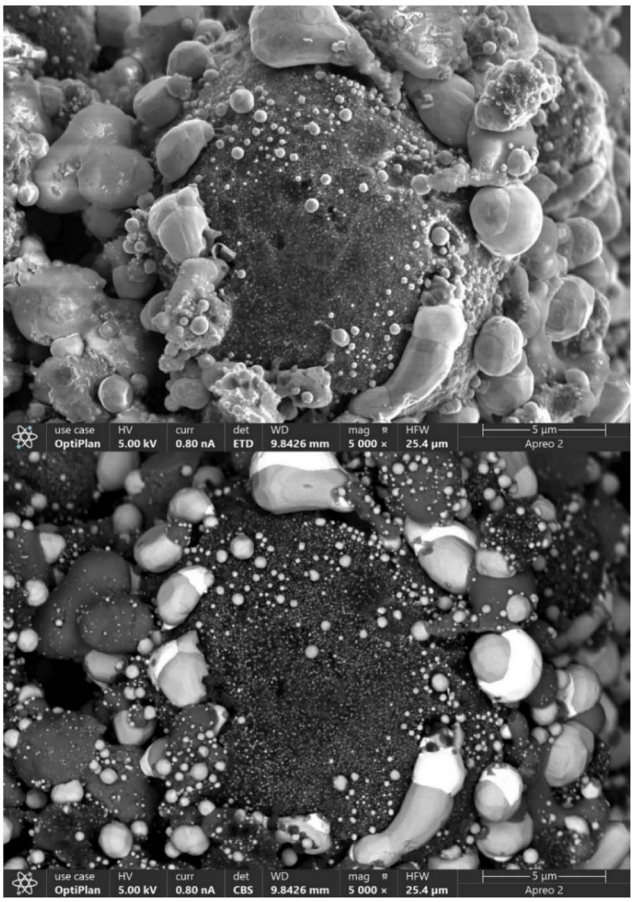

Fig. 16 SEM image of sample Ag_9Ni_{91} after the DSC analysis (top – ETD detector, bottom – CBS detector).

A SEM micrograph of Ag_9Ni_{91} nanoparticles after DSC analysis is shown in Fig. 16. Despite the high Ni content, the nickel shell of the prepared nanoparticles did not always completely encapsulate the silver core and protect it against coagulation. The image reveals that some nanoparticles located on the surface of the pyrolysis products were not sufficiently protected and coalesced into larger agglomerates. In contrast, nanoparticles embedded within the carbon matrix retained their original size, which explains the persistent melting point depression observed in all three DSC cycles as well as the broad endothermic peaks. ChemiSEM analysis (Fig. S8) shows that the surface of the smaller particles is covered with nickel, suggesting that the Ni shell in this sample predominantly formed a continuous layer. This nickel coating effectively protected the silver-rich melt inside the nanoparticles against coagulation

Table 2 Summary of organic envelope decomposition temperatures and melting temperatures of Ag–Ni NPs

Sample	Organic envelope decomposition temperatures [°C]	Melting temperature [°C]			
		(1) Cycle	(2) Cycle	(3) Cycle	Bulk material
Ag_9Ni_{91}	209.4, 240.3	951.4	951.8	951.9	AgNi – 961.1 (ref. 32)
$Ag_{51}Ni_{49}$	236.0	948.5, 958.1	950.7, 957.4	951.2, 957.2	
$Ag_{86}Ni_{14}$	240.2, 436.2	946.3, 952.7	951.9	951.6	

and sintering. However, the shell was not fully continuous for all particles, allowing the silver melt to exude onto the surface, visible in Fig. S8 as continuous pink regions. The micrograph further indicates phase separation into two conjugated phases at the microscale, *i.e.*, Ag-rich and Ni-rich domains, with their proportions determined by the Ag–Ni phase diagram. Such phase segregation and the formation of conjugated solutions were also observed in SEM images after KEMS analysis, where the fraction of the Ag-rich phase increased with increasing Ag content, in agreement with the lever rule for phase diagrams. The yellow–green regions correspond to pyrolysis products of organic compounds forming the carbon matrix. The elemental ratio obtained from EDS analysis (12 at% Ag and 88 at% Ni) is in good agreement with the ICP-OES results.

A SEM micrograph of the $Ag_{86}Ni_{14}$ sample after DSC analysis is presented in Fig. 17. The image shows that, within the examined area, the nanoparticles coalesced into a single large macro-particle. Given the high silver content, it can be assumed that the nickel shell was incomplete and did not effectively protect the silver core against coagulation. This likely resulted in the partial melting of silver and the formation of a continuous layer that covered both the pyrolysis products and the nickel-rich phase. Since a spherical morphology is energetically favorable, repeated heating and cooling cycles led to the formation of a globular macro-particle composed of the Ag-rich melt. The presence of the underlying Ni-rich phase is evidenced by the EDS mapping of nickel (Fig. S9), whereas the predominance of Ag-rich phase on the surface is confirmed by the EDS mapping of silver (Fig. S10).

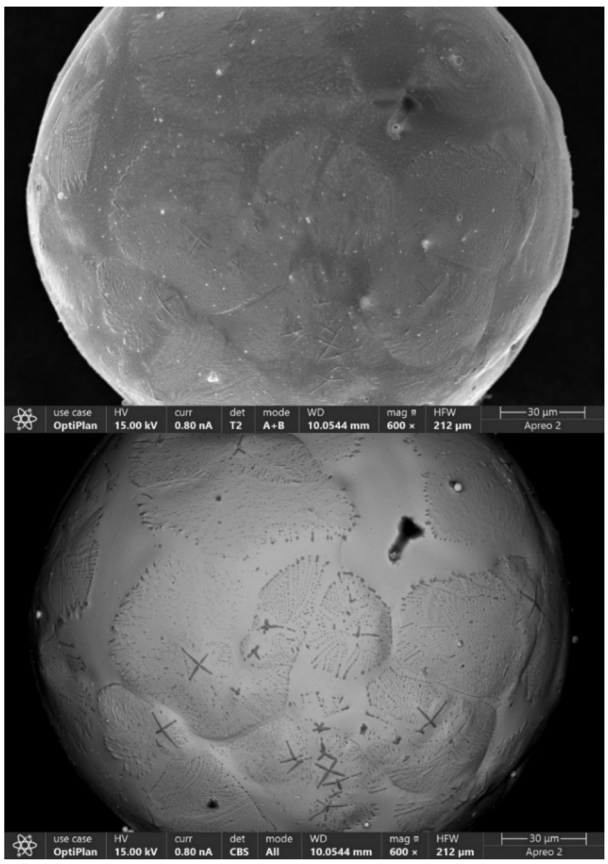

Fig. 17 SEM image of sample $Ag_{86}Ni_{14}$ after the DSC analysis (top – ETD detector, bottom – CBS detector).

SEM observations complemented by EDS analysis confirmed that, during heating, pyrolysis of the organic shell occurs, leading to the formation of a carbon matrix. Owing to the combined effect of this carbon matrix and the core–shell structure of the Ag@Ni nanoparticles, particles embedded within the matrix largely retained their morphology and size even after three heating–cooling cycles. In contrast, nanoparticles with an incomplete nickel shell located outside the matrix were prone to coagulation, resulting in the formation of larger agglomerates. This process led to the coexistence of different particle size fractions within the samples, which is manifested in the DSC curves as a broad endothermic peak in the melting temperature region.

Summary and conclusions

Bimetallic AgNi nanoparticles with a core–shell structure were synthesized with varying Ag : Ni ratios, along with elemental nanoparticles of the individual metals. The synthesized nanoparticles were characterized using UV-Vis spectroscopy to investigate the presence of surface plasmon resonance. The hydrodynamic size of the nanoparticles, including the organic shell, was determined by dynamic light scattering (DLS), while the size of the inorganic nanoparticle cores was evaluated by transmission electron microscopy (TEM) or scanning transmission electron microscopy (STEM).

The dependence of the catalytic activity of the nanoparticles on their composition was investigated using the KEMS method. Catalytic activity was primarily evaluated based on the production of carbon dioxide, and secondarily by monitoring the evolution of organic by-products formed during the thermal decomposition of the organic shell on the nanoparticle surface. The catalytic decomposition of the organic shell commenced at approximately 100 °C. The results revealed a clear dependence of catalytic activity on nanoparticle composition. The highest CO_2 production was observed for the $Ag_{35}Ni_{65}$ sample, which exhibited a substantially stronger signal compared to the other samples. In contrast, the $Ag_{29}Ni_{71}$ sample consistently showed the highest intensities of organic by-products, often by an order of magnitude greater than in other samples. Based on the obtained data, nanoparticles containing approximately 30–50 at% Ag demonstrated the highest catalytic activity. A strong CO_2 signal was also recorded for elemental Ni nanoparticles, whereas elemental Ag nanoparticles exhibited the lowest CO_2 intensity. In the case of bimetallic nanoparticles, a synergistic effect between the Ni shell and the Ag core was observed, resulting in a composition-dependent catalytic activity. However, the catalytic process on the Ag–Ni NPs is complex leading also to formation of organometallic compounds.

The thermal stability of the synthesized nanoparticles was investigated using DSC. For all three analysed samples, a decrease in melting temperature of approximately 10 °C was observed across all three heating–cooling cycles. The consistent reduction in melting temperature across the cycles is most

likely attributed to the combined effect of the core–shell structure of the Ag@Ni nanoparticles and the carbon matrix formed during heating. The latter can encapsulate the nanoparticles, preventing their aggregation into bulk material.

The state of the nanoparticles after KEMS and DSC analyses was examined using SEM and SEM-EDS. During the analysis, phase separation occurred, resulting in the formation of silver-rich and nickel-rich regions. The images show that the core–shell structure of the nanoparticles, together with the carbon matrix, effectively prevented aggregation of a portion of the nanoparticles into larger entities. However, some nanoparticles with incomplete nickel shells or located outside the carbon matrix did undergo aggregation, forming larger particles. This observation is consistent with the broad endothermic peaks observed in the DSC measurements.

Conflicts of interest

There are no conflicts to declare.

Data availability

The authors declare that the data supporting the findings of this study are available within the paper and its supplementary information (SI). Supplementary information: additional experimental information and details, EDX, STEM, SEM, XPS, mass spectra, DSC, as well as supporting figures. See DOI: https://doi.org/10.1039/d6ra01654e.

Acknowledgements

Research was supported by Czech projects MUNI/A/1691/2024 (Development of methods and instrumentation for chemical analysis and study of natural and synthetic materials, including biologically significant substances).

References

1 L. Xu, H.-W. Liang, Y. Yang and S.-H. Yu, Stability and Reactivity: Positive and Negative Aspects for Nanoparticle Processing, *Chem. Rev.*, 2018, **118**(7), 3209–3250, DOI: 10.1021/acs.chemrev.7b00208.

2 A. Yuda, A. Kumar, I. Abu Reesh, C. K. Russell, J. T. Miller, M. Ali Saleh Saad and M. J. Al-Marri, Electrooxidation of Methanol on Ag, AGNI, and AGCO Catalysts Prepared by Combustion Synthesis Technique, *Int. J. Energy Res.*, 2022, **46**(15), 22162–22175, DOI: 10.1002/er.8696.

3 M. Kumar and S. Deka, Multiply Twinned AgNi Alloy Nanoparticles as Highly Active Catalyst for Multiple Reduction and Degradation Reactions, *ACS Appl. Mater. Interfaces*, 2014, **6**(18), 16071–16081, DOI: 10.1021/am503913y.

4 R. Antony, R. Marimuthu and R. Murugavel, Bimetallic Nanoparticles Anchored on Core–Shell Support as an Easily Recoverable and Reusable Catalytic System for Efficient Nitroarene Reduction, *ACS Omega*, 2019, **4**(5), 9241–9250, DOI: 10.1021/acsomega.9b01023.

5 M. Kumar, K. Soni, G. D. Yadav, S. Singh and S. Deka, Surfactant Directed $Ag_{1-x}Ni_x$ Alloy Nanoparticle Catalysed Synthesis of Aromatic Azo Derivatives from Aromatic Amines, *Appl. Catal., A*, 2016, **525**, 50–58, DOI: 10.1016/j.apcata.2016.06.039.

6 Z.-J. Jiang, C.-Y. Liu and L.-W. Sun, Catalytic Properties of Silver Nanoparticles Supported on Silica Spheres, *J. Phys. Chem. B*, 2005, **109**(5), 1730–1735, DOI: 10.1021/jp046032g.

7 K. Wojtaszek, F. Cebula, B. Rutkowski, M. Wytrwal, E. Csapó and M. Wojnicki, Synthesis and Catalytic Study of NiAg Bimetallic Core–Shell Nanoparticles, *Materials*, 2023, **16**(2), 659, DOI: 10.3390/ma16020659.

8 T. T. K. Huynh, T. Q. N. Tran, H. H. Yoon, W.-J. Kim and I. T. Kim, AgNi@ZnO Nanorods Grown on Graphene as an Anodic Catalyst for Direct Glucose Fuel Cells, *Korean J. Chem. Eng.*, 2019, **36**(7), 1193–1200, DOI: 10.1007/s11814-019-0293-z.

9 Q.-X. Wang, M.-T. Yuan, H.-Y. Shen, H.-Y. Zhang, X. Chen, Y. Xu, X.-X. Duan, K.-L. Liu, T. Gao, Y.-G. Ning and J. Wang, Fabrication of Polyaniline-Supported Bimetal AgNi Nanoparticles and the Enhanced Performance towards Formate Oxidation, *J. Solid State Electrochem.*, 2021, **25**(4), 1197–1205, DOI: 10.1007/s10008-021-04902-4.

10 S. T. Raza Naqvi, T. Rasheed, S. Majeed, D. Hussain, B. Fatima, M. Najam Ul Haq, R. Nawaz, N. Ahmad and T. Noon, Nitrogen Doped Carbon Quantum Dots Conjugated with AgNi Alloy Nanoparticles as Potential Electrocatalyst for Efficient Water Splitting, *J. Alloys Compd.*, 2020, **847**, 156492, DOI: 10.1016/j.jallcom.2020.156492.

11 R. Nath, K. Deori and G. Borah, Visible-Light Hydrogenation of Aromatic Nitriles and Decarboxylation of Phenylacetic Acids Using a Ag–Ni@α/γ-Fe_2O_3 Magnetic Nanocatalyst, *ACS Appl. Nano Mater.*, 2026, **9**, 78–90, DOI: 10.1021/acsanm.5c03898.

12 R. Hazarika, D. Roy and K. Deori, AgNi Alloy Nanoparticles as Dual-Function Catalysts for Sustainable Nitrile Hydration and Electrocatalytic Hydrogen Generation, *ChemCatChem*, 2025, **17**, e01369, DOI: 10.1002/cctc.202501369.

13 A. R. G. Caranton, A. V. P. Lino, C. Macchiutti, J. D. Peña Serna, N. R. C. Huaman, F. Stavale, E. Annese and J. M. Assaf, Enhanced oxygen mobility in NiAg alloy catalysts for methane dry reforming: the role of AgO nanoparticles, *Catal. Today*, 2025, **455**, 115316, DOI: 10.1016/j.cattod.2025.115316.

14 P. Bräuer, F. Muench, S. Stojkovikj, S. Gupta, M. T. Mayer, W. Ensinger, C. Roth and G. A. El-Nagar, Shape-Controlled Electroless Plating of Hetero-Nanostructures: AgCuand AgNi-Decorated Ag Nanoplates on Carbon Fibers as Catalysts for the Oxygen Evolution Reaction, *ACS Appl. Nano Mater.*, 2022, **5**(8), 10348–10357, DOI: 10.1021/acsanm.2c01618.

15 J. Sun and S. L. Simon, The Melting Behavior of Aluminum Nanoparticles, *Thermochim. Acta*, 2007, **463**(1–2), 32–40, DOI: 10.1016/j.tca.2007.07.007.

16 Q. Jiang, S. Zhang and M. Zhao, Size-Dependent Melting Point of Noble Metals, *Mater. Chem. Phys.*, 2003, **82**(1), 225–227, DOI: 10.1016/S0254-0584(03)00201-3.

17 V. Vykoukal, F. Zelenka, J. Bursik, T. Kana, A. Kroupa and J. Pinkas, Thermal Properties of Ag@Ni Core-Shell Nanoparticles, *Calphad*, 2020, **69**, 101741, DOI: 10.1016/j.calphad.2020.101741.

18 P. Brož, M. Hejduková, V. Vykoukal, F. Zelenka, J. Sopoušek, J. Buršík and O. Zobač, Study of Surface Effects and Catalytic Properties of Selected Ni-Based Bimetallic Nanoparticles by Knudsen Effusion Mass Spectrometry, *Calphad*, 2019, **64**, 334–341, DOI: 10.1016/j.calphad.2019.01.013.

19 X. J. Liu, F. Gao, C. P. Wang and K. Ishida, Thermodynamic Assessments of the Ag-Ni Binary and Ag-Cu-Ni Ternary Systems, *J. Electron. Mater.*, 2008, **37**(2), 210–217, DOI: 10.1007/s11664-007-0315-1.

20 V. B. Rajkumar and S. Chen, Thermodynamic Modeling of Ag-Ni System Combining Experiments and Molecular Dynamic Simulation, *J. Electron. Mater.*, 2017, **46**(4), 2282–2289, DOI: 10.1007/s11664-016-5246-2.

21 V. Vykoukal, J. Bursik, P. Roupcova, D. A. Cullen and J. Pinkas, Solvothermal Hot Injection Synthesis of Core-Shell AgNi Nanoparticles, *J. Alloys Compd.*, 2019, **770**, 377–385, DOI: 10.1016/j.jallcom.2018.08.082.

22 O. A. Yeshchenko, I. M. Dmitruk, A. A. Alexeenko, A. V. Kotko, J. Verdal and A. O. Pinchuk, Size and Temperature Effects on the Surface Plasmon Resonance in Silver Nanoparticles, *Plasmonics*, 2012, **7**(4), 685–694, DOI: 10.1007/s11468-012-9359-z.

23 G. C. Papavassiliou, Surface Plasmons in Small Au-Ag Alloy Particles, *Met. Phys.*, 1976, **6**(4), L103–L105, DOI: 10.1088/0305-4608/6/4/004.

24 T. Kiba, K. Masui, Y. Inomata, A. Furumoto, M. Kawamura, Y. Abe and K. H. Kim, Control of Localized Surface Plasmon Resonance of Ag Nanoparticles by Changing Its Size and Morphology, *Vacuum*, 2021, **192**, 110432, DOI: 10.1016/j.vacuum.2021.110432.

25 V. Amendola, O. M. Bakr and F. A. Stellacci, Study of the Surface Plasmon Resonance of Silver Nanoparticles by the Discrete Dipole Approximation Method: Effect of Shape, Size, Structure, and Assembly, *Plasmonics*, 2010, **5**(1), 85–97, DOI: 10.1007/s11468-009-9120-4.

26 D. D. Evanoff and G. Chumanov, Synthesis and Optical Properties of Silver Nanoparticles and Arrays, *ChemPhysChem*, 2005, **6**(7), 1221–1231, DOI: 10.1002/cphc.200500113.

27 K.-C. Lee, S.-J. Lin, C.-H. Lin, C.-S. Tsai and Y.-J. Lu, Size Effect of Ag Nanoparticles on Surface Plasmon Resonance, *Surf. Coat. Technol.*, 2008, **202**(22–23), 5339–5342, DOI: 10.1016/j.surfcoat.2008.06.080.

28 P. K. Baroliya, J. Chopra, T. Pal, S. Maiti, S. A. Al-Thabaiti, M. Mokhtar and D. Maiti, Supported Metal Nanoparticles Assisted Catalysis: A Broad Concept in Functionalization of Ubiquitous C–H Bonds, *ChemCatChem*, 2021, **13**(22), 4655–4678, DOI: 10.1002/cctc.202100755.

29 M. B. Pshenitsyn, O. A. Boeva, A. S. Konopatsky, A. Yu. Antonov and K. N. Zhavoronkova, Catalysis on Mono- and Bimetallic CunAgm Nanoparticles of the Silver–Copper System, *Kinet. Catal.*, 2024, **65**(2), 188–201, DOI: 10.1134/S0023158423601158.

30 J. Sopoušek, J. Pinkas, P. Brož, J. Buršík, V. Vykoukal, D. Škoda, A. Stýskalík, O. Zobač, J. Vřešťál, A. Hrdlička and J. Šimbera, Ag-Cu Colloid Synthesis: Bimetallic Nanoparticle Characterisation and Thermal Treatment, *J. Nanomater.*, 2014, **2014**, 1–13, DOI: 10.1155/2014/638964.

31 K. Blažek, P. Brož, V. Vykoukal, L. Šimoníková, J. Sopoušek and A. Záděra, On the Thermal Stability and Surface and Catalytic Properties of Cu-Ni Nanoparticles, *Mol. Catal.*, 2025, **582**, 115188, DOI: 10.1016/j.mcat.2025.115188.

32 A. Kroupa, A. Dinsdale, A. Watson, J. Vřešťál, J. Vizdal and A. Zemanova, The Development of the COST 531 Lead-Free Solders Thermodynamic Database, *JOM*, 2007, **59**, 20–25, DOI: 10.1007/s11837-007-0084-6.